Measurement of atomic sodium release during pyrolysis and combustion of sodium-enriched Zhundong coal pellet

Zhihua Wang[1], Yingzu Liu[1,2], Ronald Whiddon[1*], Kaidi Wan[1,2], Yong He[1], Jun Xia[2], Kefa Cen[1]

[1]State Key Laboratory of Clean Energy Utilization, Zhejiang University, 310027, Hangzhou, P.R. China

[2]Department of Mechanical, Aerospace and Civil Engineering & Institute of Energy Futures, Brunel University London, Uxbridge UB8 3PH, UK

** Corresponding author: Ronald Whiddon , Tel:+86-571-87953162 , Fax:+86-571-87951616 , Email: rjwhiddon@zju.edu.cn*

Abstract Temporally resolved measurements of surface temperature, pellet diameter and proximal sodium concentration field are presented for the combustion of a high sodium coal (Zhundong) pellet. Non-resonant Planar laser-induced fluorescence (PLIF) was used to image the atomic sodium distribution around the coal pellet. The release profile of atomic sodium demonstrates three phases of combustion: (I) the devolatilization stage, (II) the char burnout stage, and (III) the ash reaction stage. Highest peak sodium concentration occurred in the char burnout stage, while the ash stage had the longest duration. The radial and axial sodium concentration decay during different phases of combustion was analyzed. During char burnout and ash stages, the maximum concentration of atomic sodium was near the pellet. In the devolatilization stage, burning of volatile-gases creates a high temperature region away from the surface of the coal pellet, which enhances the decomposition of sodium compounds in this region. Axial decay of atomic sodium concentration was governed by chemical reactions during all combustion stages. Calculation of atomic sodium flux (Na^*_{flux}) indicate that the smaller pellet releases atomic sodium more strongly in the devolatilization and char burnout stages than larger pellet. The mechanism of sodium release was inferred from the time derivatives of Na^*_{flux}, pellet-surface temperature (T) and pellet diameter (d). During the devolatilization stage, only Na^*_{flux} and T show variations, indicating that atomic sodium release is due to pyrolysis of the coal pellet. In the char burnout stage, time derivatives of the three parameters obey a common trend, indicating that the sodium release is associated with the burning of organic components in the pellet. In the ash reaction stage, T and d remain constant, indicating that the release of atomic sodium may be attributed to slow processes in the ash, likely vaporization of sodium from crystalline solids. A two-steps sodium release kinetics has been developed in this study and the simulation results agree well with measurements at three burning stages of coal pellet.

Key words: planar laser-induced fluorescence; atomic sodium; sodium release mechanism; Zhundong coal

1 Introduction

Growing energy demand has led to increased use of low rank coals, which may contain appreciable levels of contaminants. Some of these impurities, when released during coal combustion, may amass on heat transfer surfaces with adverse effects [1]. Sodium is a prime example. Various sodium compounds decompose during combustion and condense to some substance that sticks to heat transfer surfaces in the furnaces. The sodium compounds will collect fly ash and eventually cause surface degradation and lower heat transfer efficiency [2]. Zhundong coal, which is expected to provide a large share of coal consumed in China, has been found to have severe fouling and slagging problems due to its high concentration of sodium compounds [3, 4]. This issue severely limits the use of this coal reserve. Understanding the release of sodium during various stages of coal combustion is essential to develop impurity control strategies for high-impurity-coal combustion.

In general, volatile sodium in coal is differentiated into three groups [5] : water-soluble sodium (Na salts such as NaCl), organically-bound sodium (Na attached to an organic carbon structure) and insoluble sodium (Na bound within clay minerals). The first two groups are found to be releasable during combustion [5, 6] and, to a certain extent, decompose into atomic sodium [7]. Based on equilibrium calculations, atomic sodium is the favored form of sodium species within a flame environment except under high chlorine concentration conditions [8]. The final forms of sodium in post-flame gases can be modeled well using current mechanisms [7, 9, 10] and the calculation results suggest sodium chloride NaCl and sodium hydroxide NaOH are the major sodium species [7].

The behavior of sodium species during coal combustion has been studied using both offline and online measurements. Offline analysis of fuel and ash compositions continues to be used for supporting and complementing online data [11-15]. These results reveal physical and chemical characteristics of

60 sodium in the ash residues, which aids in understanding the transformations of sodium. For gas phase
61 measurement, Monkhouse et al. [16] reviewed measurements of alkali species released during coal
62 combustion using online optical diagnostic methods and mass spectrometry methods. These methods are
63 helpful in understanding different forms of sodium species when burning coal, but they do not give
64 sufficient information about the dynamics of sodium release and subsequent reactions.

65 Various laser techniques have been used to provide time-resolved measurement of alkali release
66 during coal combustion. Hartinger et al. [17, 18] used excimer laser-induced fragmentation fluorescence
67 (ELIF) to detect the in-situ sodium concentration in a pressurized fluidized-bed coal furnace. Schlosser
68 et al. [19] employed tunable diode laser absorption spectroscopy to measure time-resolved potassium
69 release in their laboratory-scale coal combustor. He et al. [20] utilized the laser-induced breakdown
70 spectroscopy (LIBS) to measure the release profile of sodium and potassium compounds directly above
71 a burning coal sample. van Eyk et al. [21, 22] developed a quantitative planar laser-induced
72 fluorescence (PLIF) technique to measure the release of atomic sodium from a burning coal sample. A
73 model of sodium release has been developed, although the devolatilization stage was not included due
74 to strong Mie scattering. To the best of our knowledge, data on the release of atomic sodium compounds
75 and its spatial distribution during the whole period of coal combustion has not been reported.

76 In our previous work, LIBS was used to measure the sodium concentration at 1 cm above a coal
77 pellet [20, 23]. These studies examined the influence of gas phase compositions [20] and the effects of
78 Na parent compounds [23] on sodium release. While these studies provided time-resolved information
79 on sodium release, only the sodium concentrations at one location were reported and all sodium
80 compounds were included in the sodium signal. This present experimental study addresses these
81 problems by using a quantitative PLIF technique [24] to provide time resolved, 2-D measurement of

atomic sodium in the gas field near a burning Zhundong coal sample. Additionally, surface temperature and pellet diameter measurements are presented. Based on these experiments, a mechanism of atomic sodium release from a burning pellet and the decay of atomic sodium as a function of the distance from the pellet can then be developed.

2 Experimental setup

A graphical 3D schematic of the experimental system is shown in Fig. 1. The coal sample was placed on parallel ceramic rods with diameter of 1 mm at 1 cm above the burner surface. A heat flux burner was used, as in our previous studies [23, 25], to provide a flat flame that ignited and sustained combustion of the coal pellet. The burner was operated with a premixed methane/air flame at an equivalence ratio of 0.8 with 0.59 SL/min methane and 7.06 SL/min air. The flame temperature was calculated to be ~1892 K at the height of the coal sample pellet. The main gas composition in the gas field was 3.9% O_2, 7.6% CO_2, 15.4% H_2O and 72.8% N_2, as calculated by CHEMKIN 3.7 with the GRI 3.0 mechanism [26].

2.1 Coal samples

The Zhundong coal sample used in PLIF tests was pressed into pellets with three different diameters. The smallest pellet weighed approximately 50 mg with a diameter of 4 mm. The other two weighed 170 mg and 360 mg with diameters of 6mm and 8 mm, respectively. The Zhundong coal used in this study was the same as our previous study [23], the chemical analysis of the raw coal and ash (prepared under 815 ^{o}C) is given in Table 1. This coal has a relatively small proportion of ash, but the sodium concentration in the ash is much higher than that of common coals as well as enriched CaO and less SiO_2 components.

2.2 PLIF systems

104 The PLIF system comprised a dye laser (Continuum, ND6000) with frequency doubling that was
105 pumped by an Nd:YAG laser (532 nm, Spectra-Physics Quanta-Ray). The wavelength of the resulting
106 laser pulse is 330.274 (5 mJ per pulse), which was used to induce fluorescence (3S→4P) from atomic
107 sodium [24]. The laser beam was formed into a 2.5 cm high laser sheet with a cylindrical lens and a
108 spherical lens. The bottom of the laser sheet (x = 0 mm) was set at the height of the ceramic rods (10
109 mm above the burner). An intensified charge coupled device (ICCD, PI MAX 3, Princeton Instrument,
110 1024 × 1024 pixel array) was used to record the fluorescence signal from the measurement region. A
111 glass camera lens (Nikkor 50mm 1:1.4D) was used, which has the additional benefit of rejecting scatter
112 from the ultraviolet excitation beam while fast gating of the ICCD (250 ns) reduced the background
113 flame emission. Two cuvettes filled with an ethanol/dye solution were positioned such that the laser
114 beam intensity was depicted before and after the Na fluorescence region. The cuvettes were used as a
115 means to provide correction of the vertical laser sheet energy distribution in the flame fluorescence as
116 well as to detect laser absorption by sodium released by the coal pellet. Moreover we also used a digital
117 camera directly imaging the appearance of the burning particle. The exposure time for imaging was
118 1/200 s.

119 **2.3 Surface temperature and pellet diameter measurement**

120 During combustion, the surface temperature of a coal pellet can be determined by two-color
121 pyrometry [22, 27]. In our study, thermal emission from the burning pellet was collected using a bioptic
122 lens attachment (LAVISION VZ-image doubler) with two filters (1 nm bandwidth) centered at 633 nm
123 and 647 nm in alternate paths of the bioptic to provide the spectral discrimination needed for two-color
124 pyrometry. Images were collected at 0.5 Hz with a gate width of 800 ms throughout the duration of the
125 coal pellet combustion. The surface temperature was measured separately from the PLIF measurement,

and each measurement was repeated five times. The 2D images of pellet thermal radiation can be used to calculate the surface temperature by using Wien's equation to compare the intensity of two wavelengths [28]:

$$T_p = \frac{C_2\left(\frac{1}{\lambda_2}-\frac{1}{\lambda_1}\right)}{\ln\frac{E_{\lambda_1}}{E_{\lambda_2}}+\ln\frac{S_{\lambda_2}}{S_{\lambda_1}}+\ln\frac{\varepsilon_{\lambda_2}}{\varepsilon_{\lambda_1}}+\ln\frac{\lambda_1^5}{\lambda_2^5}} \quad (1)$$

where T_p is the surface temperature K, C_2 is the second Planck's constant 1.4388 $cm{\cdot}K$, λ is the wavelength of thermal radiation μm, E is the emissive power $W/(cm^2{\cdot}\mu m)$, ε is the emissivity of the pellet surface and S is the system spectral response. The value of $S_{\lambda 1}/S_{\lambda 2}$ in this measurement can be calibrated by measuring a thermocouple in the flame. Moreover, since the wavelengths are very close to each other (633 nm and 647 nm), the value of $\varepsilon_{\lambda 1}/\varepsilon_{\lambda 1}$ was approximated by 1 here.

While the coal pellet was burning, strong thermal radiation made its shape clearly distinguishable [22], allowing the diameter of the pellet to be estimated by thermal radiation data. The diameter was averaged between two orthogonal dimensions in the two wavelength images.

2.4 Laser Absorption calibration and uncertainty.

The absolute atomic sodium concentrations in the calibration flame are determined using laser absorption measurements [21, 29] calculated from the Beer-Lambert equation:

$$\ln(I_{out}/I_{in}) = n\times\int_{\omega_c-b_\omega/2}^{\omega_c+b_\omega/2}\sigma(\omega)d\omega\times x \quad (2)$$

where n is the number of atoms per unit volume and $\sigma(\omega)$ is the frequency dependent absorption cross-section defined by:

$$\sigma(\omega) = \frac{h\times\omega\times B\times g(\omega)}{2\pi c} \quad (3)$$

where $g(\omega)$ is the frequency profile of the transition and the absorption coefficient B can be calculated from the spontaneous emission coefficient. The ND6000 laser has a bandwidth of 0.05 cm^{-1} (b_ω is the angular frequency value of the bandwidth), which can be used to define the integrated area with the

145 angular frequency of the laser, i.e., ω_c. The coefficient of absorption was derived in similar manner to
146 that presented in van Eyk et al. [21] The frequency profile $g(\omega)$ was estimated from the frequency
147 dependent absorption profile around 330 nm to obtain the function $f(\omega)$ which is normalized by the
148 integrated area of $f(\omega)$, a.

$$\int_{-\infty}^{+\infty} g(\omega)d\omega = 1 \tag{4a}$$

$$\int_{-\infty}^{+\infty} f(\omega)d\omega = a \tag{4b}$$

149 A stable flame sodium concentration was provided using the same burner and flame seeding
150 method which was used in our previous work to calibrate LIBS measurements [20, 21]. The frequency
151 dependent absorption profile with a Gaussian fit, $f(\omega)$ and the normalized function $g(\omega)$ are shown in
152 Fig. 2. As the full width half maximum of the transition is wider than the laser bandwidth by greater
153 than a factor of 10^4, the spectral overlap may be assumed to be equal to the transition centerline,

$$\int_{\omega_c - b_{\omega/2}}^{\omega_c + b_{\omega/2}} \sigma(\omega)d\omega \approx \sigma(\omega_c)\,. \tag{5}$$

154 From the obtained $g(\omega)$, the value of $\sigma(\omega_c)$ was determined to be 5.6310×10^{-19} /(N•m^2), where N is
155 the number density of atomic sodium.

156 **2.4.1 Fluorescence measurements**

157 Quantitative measurement of sodium distribution in the region above the burning coal pellet was
158 accomplished through combination of simultaneous laser absorption and laser fluorescence techniques.
159 As discussed above, each image frame included the laser induced fluorescence signal arising from
160 sodium excited by the 330 nm radiation as well as laser sheet energy measured by passing the laser
161 sheet through dilute ethanol/dye filled quartz cuvettes prior to and after transiting the measurement
162 region. Briefly, the data processing proceeded thus:

163 • Blank measurements of a flame without any coal pellet and the laser tuned to the sodium

transition were collected. From these measurements it was possible to measure the electronic background signal (709 counts ± 5.5%) and the average flame luminescence. The blank values were subtracted from subsequent measurements.

- Background measurements of the coal pellet and flame were collected for the duration of a coal fluorescence measurement. The laser was tuned away from the 330 nm sodium transition during the measurement in order to assess signal loss not coming from sodium absorption processes, e.g., scattering, photofragmentation (NaOH), and competing fluorescence. The height of the laser sheet was determined from the vertical distribution in the post-flame cuvette (I_{out}); to avoid error from changing pellet size, the sheet height measure in the first few seconds of combustion was used to define the laser sheet height. The laser intensity before and after passing through the plume emitted above the burning coal pellet was calculated by the intensity of signal in the first (I_{in}) and second (I_{out}) cuvettes (summed vertically, averaged horizontally), being certain of proper alignment and dimension of the laser sheet in each cuvette. The calculated ratio of (I_{out}/I_{in}) for the background was normalized with an estimated value at 0% absorption; the result was used in Eq. (2), with a path length of 0.02 m, to calculate the background calculated concentration, shown in Fig. 3. The background calculated concentration is greatest in the first few seconds of the devolatilization stage which we attribute to absorption by devolotalization species and scatter from large particles released from the pellet. During this time there was noticable fluorescence in the first few millimeters directly above the coal pellet. After approximately 30 seconds no further fluorescence was visible. The background calculated concentration similarly increased slightly during the char combustion phase which may be due to the presence of NaOH which photofragments at this

wavelength [30]. The error in the calculated concentration during ash stage would likely come from photofragmentation of NaOH and as well as spurious scatter and absorbance. The standard deviation measured during the ash stage for offline measurement is 5.69 %, or 0.08 ppm.

- Online measurements of the flame with coal pellet were collected and multiple runs performed to verify consistency of the result. The values for I_{out} and I_{in} are collected in the same way as detailed in the background measurement step. The ratio I_{out}/I_{in} is normalized against an extrapolated zero absorption ratio. This zero absorption ratio was determined by plotting I_{out}/I_{in} during the ash stage versus fluorescence intensity above the centerline, a linear fit of the data predicts the expected I_{out}/I_{in} ratio when the fluorescence signal is zero. The corrected I_{out}/I_{in} ratio was used in Eq. (2) with a path length of 0.02 m to determine the measured sodium absorption. The background calculated concentration from the preceding step was subtracted from the online measurement; the resulting values from a 4 mm pellet case are shown in Fig. 3. The calculated standard deviation measured during the ash stage for online measurement is 0.13 ppm which appears consistent with the scatter found in the earlier stages.
- Measurements of sodium fluorescence that were taken simultaneous with the absorption measurements were used to determine the spatial distribution of sodium above the pellet. The region of the ICCD images that contained the flame were cropped to include an area slightly wider than the flame, with the vertical extent that coincided with the height of the laser sheet as defined in the background measurement step. The flame images were individually corrected for laser sheet energy distribution by dividing with the normalized laser profile of the respective shot, as recorded by the first cuvette (I_{in}). Next, the flame images were normalized

by the average pixel intensity in a given frame and then multiplied by the corresponding sodium concentration for that shot as calculated in the online measurement step. Images of quantitative sodium distributions are shown in Fig. 4. The temporal profile of the sodium concentration at 14 mm above the coal pellet is shown below in Fig. 5, the standard deviation calculated during the ash stage for temporal measurement is 0.21 ppm.

3 Results and discussion

3.1 Atomic sodium spatial distribution.

The photographs and the respective Na concentration distributions recorded during the three characteristic combustion stages for the 4-mm coal pellet are presented in Fig. 4. In the devolatilization stage, a small flame appears (Fig. 4a) due to the combustion of polycyclic aromatic hydrocarbons [31], which can be clearly identified by the soot black-body emission. Subsequently, the char combustion increases the pellet temperature and strengthens thermal emission from the pellet (Fig. 4b). When all the organic components of the coal pellet have burnt away, the ash residue stays in the high temperature burnt-gas region of the burner, reaching thermal equilibrium (Fig. 4c). The 2-D Na concentration from single-shot PLIF imaging recorded at the same combustion time period as in the ICCD images are shown in Figs. 4 e-g. The atomic sodium concentration decays with the distance from the coal pellet in both the axial and radial directions due to dilution by surrounding gases and chemical reaction [22, 32]. Among the three periods of combustion, in the char burning period the instantaneous atomic sodium concentration is the highest, and in the ash period the lowest. It should be noted that by using non-resonant PLIF, it was possible to measure the atomic sodium concentration during the devolatilization period, avoiding noise from Mie scattering [21, 22, 32].

By plotting the atomic sodium concentration ($[Na]$) at x = 14 mm and r = 0 mm above the 4-mm

coal pellet over the duration of the coal sample combustion, the time history of atomic sodium release is presented in Fig. 5. The Mie scattering strongly interfere with the fluorescent signal at the initial burning stage in the 589 nm LIF measurement by van Eyk et al. [21]. However in our 330 nm measurement, the devolatilization stage, which has also been noticed in our previous LIBS results, can be clearly identified. The shape of this profile is similar to our previous LIBS measurements, which showed total sodium release [20, 23]. The three characteristic combustion stages are readily identified [22]: (I) a volatile release stage (t: 0 - 53 s, peak: 30 s) , (II) a char burnout stage (t: 54 - 453 s, peak: 394 s) and (III) an ash reaction stage (t: 454 - 4613 s). It can be seen that the devolatilization stage has the shortest duration; the ash stage is the longest; in the char burnout stage the peak sodium concentration is the highest.

3.2 Variation of atomic sodium along axial and radial distances

As mentioned in section 3.1, the atomic sodium concentration decays along the axial and radial distances; examination of the signal decay at various combustion stages can help identify the mechanism of atomic sodium variation. The [*Na*] above the pellet centerline, normalized by the [*Na*] at x = 4 mm ($[Na]_{4mm}$), the upper surface of the 4 mm pellet, is shown in Fig. 6a. Two different spatial concentration profiles can be distinguished in this plot. One such profile is seen for t = 30 s, the devolatilization stage, where [*Na*] increases axially until x = 6.5 mm, after which the signal decays. The other profile type is seen for the char burnout stage and the ash reaction stage. In these stages, [*Na*] declines continuously from the top of the pellet (x = 4 mm). In Fig. 6b, the x-derivatives of the normalized values amplify the difference between the two types of spatial concentration profiles. The opposite signs of the two groups at x = 4 mm indicates different starting slopes; additionally, the inflection point noted at the top of the measurement zone can be identified between x = 17 mm - 20 mm. At the top of the measurement zone, all the curves bend again, which may be caused by the diffusion

253 between the gas and air.

254 The radial distributions of the atomic sodium concentration during the combustion of the 4-mm
255 coal pellet are shown in Fig. 7. [*Na*] are normalized by [*Na*] on the centerline ($[Na]_c$). Considering the
256 change in [*Na*] profiles with the height, the radial distributions of the atomic sodium concentration are
257 presented at two heights: 6 mm and 10 mm. At the higher position (x = 10 mm), the profiles show the
258 same trend in different combustion stages. On the contrary, at the lower position (x = 6 mm), the radial
259 position where [*Na*] begins to decrease is clearly different in different combustion stages. The char
260 burnout stage has the widest horizontal extent and the ash stage has the narrowest one. The radial profile
261 in the devolatilization stage starts with an initial sharp decline until r≈2.5 mm, at which [*Na*] stabilizes
262 and then decreases as the profiles in the other two stages. Fig. 4a shows a small flame on the top of the
263 pellet, which leads to a local high temperature region that is absent in the other two combustion stages.
264 In this flame, volatile sodium such as NaCl, NaOH etc. which evaporate from the coal pellet will
265 decompose and generate atomic sodium [9].

266 The axial [*Na*] profiles at two time instants (t = 30 s and t = 394 s) are investigated to determine if
267 the decay of the atomic sodium concentration with x is governed by chemical reactions, diffusion or
268 both. A simple chemical reaction model and a diffusion model are employed to determine the [*Na*]
269 decay mechanism of the different profiles. According to [9, 21, 22], if the decay of the atomic sodium
270 concentration along the axial distance is governed by chemical reactions, the [*Na*] profile can be
271 described by the following equation:

$$\ln\left(\frac{[Na]}{[Na]_p}\right) = -k \times x + A \tag{6}$$

272 where A and k (mm^{-1}) are constants and $[Na]_p$ is the concentration of atomic sodium around the pellet
273 surface. If the decay of the atomic sodium concentration is governed by diffusion, there is a simplified

diffusion model [32-34] can be used to model the decay, which assumes the combustion in proximity to the coal sample can be regarded as a round jet flame and the flat flame is a co-flow. In this case, $[Na]_p/[Na]$ versus x will have a linear response characterized by the following equation:

$$\frac{[Na]_p}{[Na]} = \frac{C \times (x - x')}{r'} \tag{7}$$

where r' is the radius of the pellet, x' is the virtual origin and C is the axial decay constant. Fig. 8 presents the fitted curves determined by Eqs. (6) and (7) for the $[Na]$ profiles at two specified time instants during the combustion of the 4-mm coal pellet. Fig. 8a shows the results at t = 30 s, and Fig. 8b shows the results at t = 394 s. In both of the two figures, the plots of $\ln([Na]/[Na]_p)$ versus x can be approximated by Eq. (6) excluding a few points near x = 20 mm, implying that the decay of $[Na]$ vertically above the coal pellet is dominated by chemical reactions. From the plots of $[Na]_p/[Na]$ versus x, a linear relationship can be found after x = 20 mm at both t = 30 s and t = 394 s as expected from a diffusion model. So the decay of atomic sodium released from the pellet was first dominated by chemical reaction and then diffusion. After x = 20 mm, the decay will still be partly affected by chemical reaction even it does not play the dominating role, therefore the fitting of the diffusion model is not perfect. Moreover, the chemical reaction model does not fit well with the experiment data at t = 30 s when x < 6 mm. Since at t = 30 s the burning of volatile above the particle will generate atomic sodium from other sodium species and the decay-chemical-reaction-model cannot predict this phenomenon well.

3.3 Atomic sodium flux, temperature and diameter of coal pellets

The relationship between the atomic sodium release and the coal pellet combustion is investigated in this section by measuring sodium flux, surface temperature and the pellet diameter for coal pellets of 4-, 6- and 8-mm diameters. The fitting results of $[Na]$ measurements from these pellets at a specific point above the burning pellet (x = 14 mm, r = 0 mm) is shown in Fig. 9a. Moreover, the amount of

296 atomic sodium passing through a given height at any given time is the atomic sodium flux, $Na^*_{flux,t}$. It
297 can be determined as [32]:

$$Na^*_{flux,t} = 2\pi \int_0^\infty u \times [Na]_t \times r \times dr \quad (8)$$

298 where u is the gas phase velocity (m/s), which can be calculated based on the gas flow rates and
299 corrected by temperature. The amount of atomic sodium released in any given period can be determined
300 by integrating $Na^*_{flux,t}$ over the period. The zone used for integration was based on the spatial
301 distribution of atomic sodium. The height of x = 23 mm was used because the diffusion became
302 dominant from here. The integration in the radial direction was chosen from 0 mm to 15 mm to include
303 all the released atomic sodium in the gas phase. The $Na^*_{flux,t}$ in three different stages of different pellets
304 are shown in Fig. 9b. As the atomic sodium distribution in the gas phase is closely related to its flux, the
305 curves in Fig. 9a and 9b are similar to each other. With the change of the pellet diameter, the most
306 obvious result is that the release of atomic sodium is delayed for larger pellets. For both the
307 devolatilization stage and the char burnout stage, the peak value is lower for larger particles, and the
308 time of the stages becomes longer. The integrations of $Na^*_{flux,t}$ in the devolatilization and char burnout
309 stage are shown in Table 2. A larger pellet contains more sodium, so it has a larger amount of atomic
310 sodium released than the smaller pellets. However, as the release of atomic sodium can be evidently
311 affected by the pellet temperature [22, 35], the smaller pellets have a higher value of atomic sodium
312 released per unit mass in these two stages, since they are heated faster than the large pellets.

313 The time history of the surface temperature (T) and the pellet diameter (d) for the three different
314 initial pellet diameters are plotted in Fig. 10. As can been seen, the profile of surface temperature is
315 similar to the temporal profile of sodium release. The trend in the surface temperature profiles can be
316 described as follows: first, the volatile released during the devolatilization stage and burning near the

317 surface of the coal pellet quickly heats up the pellet. In the second stage, the char starts to react with
318 oxygen in the co-flow, which increases the surface temperature. In the second stage, the char starts to
319 react with oxygen in the co-flow, which increases the surface temperature. After large proportion of the
320 coal char has been oxidized, the temperature change inverts as the last of the char is scavenged. In the
321 corresponding time period the diameter of the coal pellet is essentially constant. This is because little
322 char has been burnt by this time since the char reaction is inhibited by the ash layer [36], and the surface
323 temperature decreases through heat exchange to surroundings. The 4-mm pellet has the highest
324 temperature both in the char burnout stage and ash reaction stage, since the larger pellet has stronger
325 thermal radiation and the small pellet has a smaller specific surface area.

326 The statistics regarding the time of transitions between the different combustion stages and the
327 position of local maxima are given in Table 3. From the table it can be observed that the delay of
328 initiation for the combustion stages and local maxima increase with the pellet physical dimension. The
329 increase in duration of stages is primarily the consequence of the greater mass of material. When
330 comparing the event timings for a single pellet size, a significant trend may be noted; there is a
331 discrepancy between surface temperature and sodium release regarding the location of maxima and the
332 anticipated transition between stages. This is most evident for the 8 mm coal pellet, where the peak Na
333 release is recorded approximately two minutes prior to the peak surface temperature. Comparing trends
334 of sodium release and surface temperature for the 8 mm pellet (Figs. 9 and 10), it is seen that the sodium
335 release does indeed occur earlier, and also that the peak is much less pronounced for sodium than for
336 surface temperature. van Eyk, et al. have shown that the sodium release is coupled to temperature in
337 sodium release from brown coal [22]; however, from our results it appears that sodium release may be
338 less directly indicated by pellet temperature when the coal char reaches the final stages of burnout.

Examining the difference in the coal compositions of Loy Yang coal [32] and Zhundong coal (Table 2), there is a much higher proportion of inert matter in Zhundong coal. The adsorption of sodium by compounds in the inert matter, e.g., aluminosilicates, is one possible explanation for the differences noted in the temperature and sodium release trends [37, 38]. A universal model of sodium release during coal combustion will need to account for the influence of sodium retaining materials that influence processes governing sodium release.

To further analyze the relationship between the atomic sodium flux, surface temperature and pellet diameter, their derivatives, i.e., $dNa^*_{flux,t}/dt$, dT/dt and dd/dt, for the 4-mm particle are plotted in Fig. 11. Fig. 11 shows the detailed trends for 0-600 s, in which two obvious abrupt transitions can be seen.

First we focus on the early transition. In this stage, the pellet has just been put into the hot gas field, so it experiences devolatilization. Heating due to the burning volatile gas and the hot co-flow from the burner causes a large dT/dt. Over the same time period dd/dt is almost zero, indicating that the pellet is experiencing outgassing but little char has been burnt during this period. The positive value of $dNa^*_{flux,t}/dt$ is due to physical and chemical reactions of Na compounds in the volatile phase. At the later transition, all the three variables show a considerable change in time. The dd/dt changes from an increasing negative value to around zero, indicating that most char in the pellet has been burnt out and the pellet size becomes stable. Both dT/dt and $dNa^*_{flux,t}/dt$ are changing from positive to negative values, which means both the atomic sodium concentration and surface temperature begin to decrease. After 600 s, $dNa^*_{flux,t}/dt$ and dd/dt retain a small positive value while dT/dt is stable at zero, which suggests that the temperature of the coal particle has reached equilibrium with the surrounding co-flow, although there still exist some weak reactions inside the pellet. Even though these reactions are very weak, van Eyk et al. [32] pointed out that almost three times as much sodium can be released during the

ash stage as in the char stage. The consistency of these results indicates that the sodium release is linked to specific phenomena that occur during coal pellet combustion. The relationship between the sodium release, pellet temperature and pellet diameter can be useful for modeling [35] the release of atomic sodium during the Zhundong coal combustion.

3.4 Two-steps sodium release kinetics

van Eyk et al. [35] has established a relationship between the rate of sodium release and char temperature in char burnout stage, which obeys the Arrhenius expression:

$$\begin{cases} Na^{*}_{flux,t} = Q_{Na} \times k \\ Q_{Na} = \int_{0}^{\infty} Na^{*}_{flux,t} dt \\ k = A \times \exp(-E / (R \times T)) \end{cases} \tag{9}$$

where Q_{Na} is the total atomic sodium, k is the chemical rate constant for sodium release, A is pre-exponential factor for sodium release, E is activation energy for sodium release and R is the universal gas constant, 8.314 J/(mol•K). Based on their assumption, all the sodium in the coal is releasable and the temperature distribution in char particle is uniform. Verification of this sodium release kinetics is presented here. By using our experiment results (such as T and initial sodium etc.) mentioned above, we can get the sodium release kinetics of Zhundong coal pellet as follow:

$$k = 6891 \times \exp(\frac{-228\ kJ\ /\ mol}{R \times T}) \tag{10}$$

The comparisons between experimental and simulation results are shown in Fig. 12. The simulation results agree well with the tendency of the sodium release and perform well in the char burnout and ash reaction stage. However, at the initial combustion stage, the simulation results are insufficient to predict the rate of atomic sodium release. As discussed in section 3.1, coal pellet was going through the outgassing process. So the release of atomic sodium is not only the result of combustion following Arrhenius equation but also being influenced by the pyrolysis of coal pellet. This indicates that the

mechanisms of atomic sodium release at the initial combustion stage should consider both the effect of coal burning and outgassing. In order to describe this, we built a two-steps kinetics to separately calculate the release of volatile sodium and organic sodium release when the coal pellet is burning. We assumed that the k_2 in Eq. (11) is equal to the k in Eq. (10) and the type of different Q_{Na} is calculated based on the chemical analyses in Table 1. The equations of the two-steps kinetics are:

$$\begin{cases} Na^{*}_{flux} = Q_{Na,volatile} \times k_1 + Q_{Na,char\&ash} \times k_2 \\ Q_{Na,volatile} = Q_{Na} \times Volatile \\ Q_{Na,char\&ash} = Q_{Na} \times (FixCarbon + Ash) \\ k_1 = A_1 \times \exp(-E_1 / (R \times T)) \\ k_2 = A_2 \times \exp(-E_2 / (R \times T)) \end{cases} \tag{11}$$

where $Q_{Na,volatile}$ is the total atomic sodium in the volatile matter and $Q_{Na,char\&ash}$ is the total atomic sodium in both the char and ash. *Volatile*, *FixCarbon* and *Ash* are the content of volatile matter, fixed carbon and ash in the coal (Table 1). By recalculating the atomic sodium flux based on the two-steps kinetics, the value of k_2 can be determined as:

$$k_2 = 17900 \times \exp(\frac{-198\ kJ / mol}{R \times T}) \tag{12}$$

The two-steps kinetics agrees better with the experimental results and it can successfully predict the sodium release at the initial burning stage. In general, the two-steps kinetics can predict the atomic sodium release in whole combustion period of a single coal pellet.

4 Conclusions

An experimental method for quantitative measurement of atomic sodium concentrations in the plume, the surface temperature and pellet diameter simultaneously of a burning Zhundong coal pellet has been presented. Utilization of a 330-nm laser avoids complication of Mie scattering during the initial pyrolysis stage of coal combustion, so the release and distribution of atomic sodium around the coal pellet throughout the whole combustion period has been measured. The temporal profile of the

398 release of atomic sodium can be clearly separated into three stages, two of which feature prominent
399 peaks: one peak in the devolatilization stage and the other peak in the char burnout stage. The char
400 burning features the highest instantaneous concentration of atomic sodium and the ash stage the longest
401 duration of atomic sodium release.

402 Four specific time instants were chosen to analyze the decay of atomic sodium concentrations
403 along the plume centerline and in the radial direction. The maximum concentration of atomic sodium is
404 found on the surface of the pellet in the majority of the pellet-burning period, except during the
405 devolatilization stage. The burning of volatile causes an extreme high temperature region which
406 increases the decomposition of volatile sodium compounds into atomic sodium. This causes [*Na*] to rise
407 initially before declining in the axial direction. For all stages of coal pellet combustion, the decay of the
408 atomic sodium concentration in the axial direction is found to be governed by chemical reactions.

409 The results of burning of coal pellets of all the three different diameters imply that sodium release
410 is closely related to the temperature and diameter of the pellet. The large pellet has a larger amount of
411 atomic sodium released in the devolatilization and char burnout stages. However the release of atomic
412 sodium in a smaller pellet is stronger per unit mass. The time derivatives of Na^*_{flux}, T and d reflects the
413 mechanism of sodium release can also be separated into three stages: (I) In the devolatilization stage,
414 only Na^*_{flux} and T evidently change, indicating that atomic sodium in this stage are coming out with
415 volatile through pyrolysis; (II) In the char burnout stage, the derivatives of the three parameters have the
416 same tendency, meaning the atomic sodium release is related to the burning of organic components in
417 the pellet; (III) In the ash stage, the temperature and the diameter are almost constant, so the release of
418 atomic sodium is attributed to some weak reactions in the ash. Based on the aforementioned conclusions,
419 a two-steps sodium release kinetics which separately considered different types of sodium and defined

two sets of chemical rate constants are developed. The simulation results successfully predict the atomic sodium release at the initial burning stage and agree well with the measurement results for the whole burning period of the coal pellet.

Acknowledgements

This work was support by the National Natural Science Foundation of China (51422605) and Ph.D. Programs Foundation of Ministry of Education of China (20130101110095).

Reference

[1] R.W. Bryers, Fireside slagging, fouling, and high-temperature corrosion of heat-transfer surface due to impurities in steam-raising fuels, Prog. Energy Combust. Sci. 22 (1996) 29-120.

[2] M. Neville, A.F. Sarofim, The fate of sodium during pulverized coal combustion, Fuel 64 (1985) 384-390.

[3] H. Zhou, B. Zhou, H. Zhang, L. Li, Behavior of Fouling Deposits Formed on a Probe with Different Surface Temperatures, Energy Fuels 28 (2014) 7701-7711.

[4] H. Zhou, B. Zhou, L. Li, H. Zhang, Experimental Measurement of the Effective Thermal Conductivity of Ash Deposit for High Sodium Coal (Zhun Dong Coal) in a 300 KW Test Furnace, Energy Fuels 27 (2013) 7008-7022.

[5] S.A. Benson, P.L. Holm, Comparison of inorganics in three low-rank coals, Ind. Eng. Chem. Res. 24 (1985) 145-149.

[6] J. Zhang, C.-L. Han, Z. Yan, K. Liu, Y. Xu, C.-D. Sheng, W.-P. Pan, The Varying Characterization of Alkali Metals (Na, K) from Coal during the Initial Stage of Coal Combustion, Energy Fuels 15 (2001) 786-793.

[7] L.J. Wibberley, T.F. Wall, Alkali-ash reactions and deposit formation in pulverized-coal-fired boilers: the thermodynamic aspects involving silica, sodium, sulphur and chlorine, Fuel 61 (1982) 87-92.

[8] S. Srinivasachar, J.J. Helble, D.O. Ham, G. Domazetis, Ash Deposition A kinetic description of vapor phase alkali transformations in combustion systems, Prog. Energy Combust. Sci. 16 (1990) 303-309.

[9] P. Glarborg, P. Marshall, Mechanism and modeling of the formation of gaseous alkali sulfates, Combust. Flame 141 (2005) 22-39.

[10] A.J. Hynes, M. Steinberg, K. Schofield, The chemical kinetics and thermodynamics of sodium species in oxygen - rich hydrogen flames, J. Chem. Phys. 80 (1984) 2585-2597.

[11] R.J. Quann, M. Neville, M. Janghorbani, C.A. Mims, A.F. Sarofim, Mineral matter and trace-element vaporization in a laboratory-pulverized coal combustion system, Environ. Sci. Technol. 16 (1982) 776-781.

[12] H. Oleschko, A. Schimrosczyk, H. Lippert, M. Müller, Influence of coal composition on the release of Na-, K-, Cl-, and S-species during the combustion of brown coal, Fuel 86 (2007) 2275-2282.

[13] T. Takuwa, I. Naruse, Detailed kinetic and control of alkali metal compounds during coal combustion, Fuel Process. Technol. 88 (2007) 1029-1034.

[14] S.H. LEE, F. Teats, W. Swift, D. Banerjee, SHORT COMMUNICATION Alkali-Vapor Emission from PFBC of Illinois Coals, Combust. Sci. Technol. 86 (1992) 327-336.

[15] B.N. Barman, V.L. Cebolla, A.K. Mehrotra, C.T. Mansfield, Petroleum and coal, Anal. Chem. 73 (2001) 2791-2804.

[16] P. Monkhouse, On-line diagnostic methods for metal species in industrial process gas, Prog. Energy Combust. Sci. 28 (2002) 331-381.

[17] F. Greger, K.T. Hartinger, P.B. Monkhouse, J. Wolfrum, H. Baumann, B. Bonn, In situ alkali concentration measurements in a pressuried, fluidized-bed coal combustor by excimer laser induced fragmentation fluorescence, Symposium (International) on Combustion 26 (1996) 3301-3307.

[18] K.T. Hartinger, P.B. Monkhouse, J. Wolfrum, H. Baumann, B. Bonn, Twenty-Fifth Symposium (International) on CombustionDetermination of flue gas alkali concentrations in fluidized-bed coal combustion by excimer-laser-induced fragmentation fluorescence, Symposium (International) on Combustion 25 (1994) 193-199.
[19] E. Schlosser, T. Fernholz, H. Teichert, V. Ebert, In situ detection of potassium atoms in high-temperature coal-combustion systems using near-infrared-diode lasers, Spectroc. Acta Pt. A-Molec. 58 (2002) 2347-2359.
[20] Y. He, J. Zhu, B. Li, Z. Wang, Z. Li, M. Aldén, K. Cen, In-situ Measurement of Sodium and Potassium Release during Oxy-Fuel Combustion of Lignite using Laser-Induced Breakdown Spectroscopy: Effects of O2 and CO2 Concentration, Energy Fuels 27 (2013) 1123-1130.
[21] P.J. van Eyk, P.J. Ashman, Z.T. Alwahabi, G.J. Nathan, Quantitative measurement of atomic sodium in the plume of a single burning coal particle, Combust. Flame 155 (2008) 529-537.
[22] P.J. van Eyk, P.J. Ashman, Z.T. Alwahabi, G.J. Nathan, Simultaneous measurements of the release of atomic sodium, particle diameter and particle temperature for a single burning coal particle, Proc. Combust. Inst. 32 (2009) 2099-2106.
[23] Y. He, K. Qiu, R. Whiddon, Z. Wang, Y. Zhu, Y. Liu, Z. Li, K. Cen, Release characteristic of different classes of sodium during combustion of Zhun-Dong coal investigated by laser-induced breakdown spectroscopy, Chin. Sci. Bull. 60 (2015) 1927-1934.
[24] N. Gorbunov, P. Kozłowski, K. Nowak, T. Stacewicz, Fluorescence of Sodium Vapour Excited by 330 nm Laser Pulses, Acta Phys. Pol. A 99 (2001) 531-537.
[25] W.B. Weng, Z.H. Wang, Y. He, R. Whiddon, Y.J. Zhou, Z.S. Li, K.F. Cen, Effect of N2/CO2 dilution on laminar burning velocity of H2–CO–O2 oxy-fuel premixed flame, Int. J. Hydrog. Energy 40 (2015) 1203-1211.
[26] G.P. Smith, D.M. Golden, M. Frenklach, N.W. Moriarty, B. Eiteneer, M. Goldenberg, C.T. Bowman, R.K. Hanson, S. Song, W.C. Gardiner Jr, GRI 3.0 Mechanism. <http://www.me.berkeley.edu/gri_mech>.
[27] Y. Huang, Y. Yan, G. Riley, Vision-based measurement of temperature distribution in a 500-kW model furnace using the two-colour method, Measurement 28 (2000) 175-183.
[28] W.L. Saw, G.J. Nathan, P.J. Ashman, Z.T. Alwahabi, M. Hupa, Simultaneous measurement of the surface temperature and the release of atomic sodium from a burning black liquor droplet, Combust. Flame 157 (2010) 769-777.
[29] J.E. Sansonetti, W. Martin, S. Young, Handbook of basic atomic spectroscopic data, Carbon 100 (2005) 1634.
[30] B.L. Chadwick, P.G. Griffin, R.J. Morrison, Quantitative detection of gas-phase NaOH using 355-nm multiple-photon absorption and photofragment fluorescence, Appl. Spectrosc. 51 (1997) 990-993.
[31] P.A. Bejarano, Y.A. Levendis, Single-coal-particle combustion in O2/N2 and O2/CO2 environments, Combust. Flame 153 (2008) 270-287.
[32] P.J. van Eyk, P.J. Ashman, Z.T. Alwahabi, G.J. Nathan, The release of water-bound and organic sodium from Loy Yang coal during the combustion of single particles in a flat flame, Combust. Flame 158 (2011) 1181-1192.
[33] H.A. Becker, H.C. Hottel, G.C. Williams, The nozzle-fluid concentration field of the round, turbulent, free jet, J. Fluid Mech. 30 (1967) 285-303.
[34] W.L. Saw, G.J. Nathan, P.J. Ashman, Z.T. Alwahabi, Assessment of the release of atomic Na from a burning black liquor droplet using quantitative PLIF, Combust. Flame 156 (2009) 1471-1479.
[35] P.J. van Eyk, P.J. Ashman, G.J. Nathan, Mechanism and kinetics of sodium release from brown coal char particles during combustion, Combust. Flame 158 (2011) 2512-2523.
[36] R. Hurt, J.-K. Sun, M. Lunden, A Kinetic Model of Carbon Burnout in Pulverized Coal Combustion, Combust. Flame 113 (1998) 181-197.
[37] G. Li, C.a. Wang, Y. Yan, X. Jin, Y. Liu, D. Che, Release and transformation of sodium during combustion of Zhundong coals, J. Energy Inst. 89 (2016) 48-56.
[38] W. Punjak, F. Shadman, Aluminosilicate sorbents for control of alkali vapors during coal combustion and gasification, Energy Fuels 2 (1988) 702-708.

Table 1. The chemical analysis of Zhundong coal and ash

Proximate analysis (wt.%, dry basis)									
Volatile			*Fixed carbon*			*Ash*			
30.86			64.79			4.34			
Ultimate analysis (wt.%, dry basis)									
C_d		H_d		N_d		S_d		O_d	
75.39		3.48		1.19		0.42		15.19	
Ash composition (wt.%)									
SiO_2	Al_2O_3	CaO	MgO	Fe_2O_3	Na_2O	K_2O	TiO_2	SO_3	MnO
10.79	9.62	36.83	9.21	3.95	3.42	0.4	0.68	24.74	0.35

Table 2. Cumulative mass of atomic sodium release in different combustion stages

		atomic sodium released (mg)	normalized by pellet mass (mg/g)
devolatilization stage	4 mm	1.52E-03	3.04E-05
	6 mm	1.71E-03	1.07E-05
	8 mm	1.92E-03	5.33E-06
char burnout stage	4 mm	3.03E-03	6.08E-05
	6 mm	4.42E-02	2.76E-04
	8 mm	5.11E-02	1.42E-04

Table 3. Significant points in the temporal profiles of sodium concentration, coal surface temperature and pellet diameter

Variable	Combustion stages	4mm		6 mm		8 mm	
		duration (s)	peak (s)	duration (s)	peak (s)	duration (s)	peak (s)
$Na^*_{flux,t}$	first stage	0 - 53	30	0 - 73	39	0 - 154	58
	second stage	54 - 453	394	74 -1011	763	155 -1504	946
	third stage start	454 s		1012 s		1505 s	
Temperature	first stage	0 - 61	37	0 - 87	35	0 -133	65
	second stage	62 - 485 s	397	88 - 1029	820	134 -1538	1107
	third stage start	486 s		1030 s		1539 s	
diameter	inflection point	508 s		971 s		1502 s	

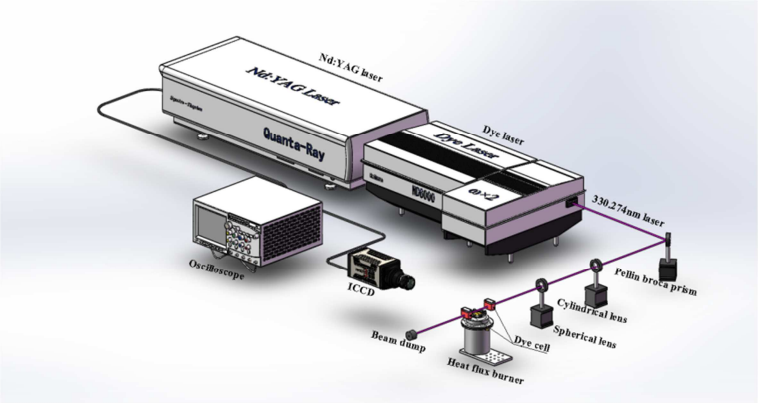

Fig. 1. The configuration of laser and detector for PLIF measurements.

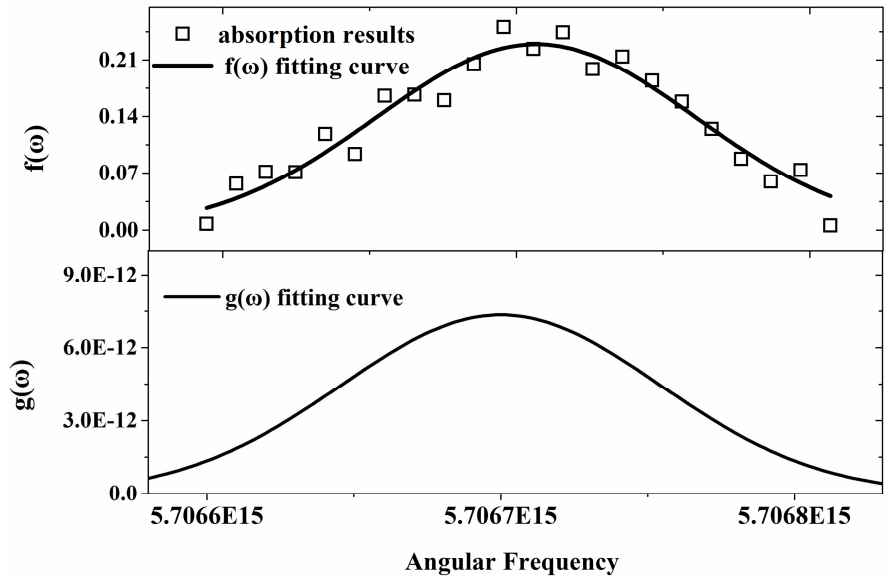

Fig. 2. Absorption cross-section evaluation from experimental measurements. Upper image is measured absorption as a function of laser angular frequency fitted with Gaussian curve, $f(\omega)$; lower image is the normalized absorption, $g(\omega)$, from which the absorption cross-section at ω is determined.

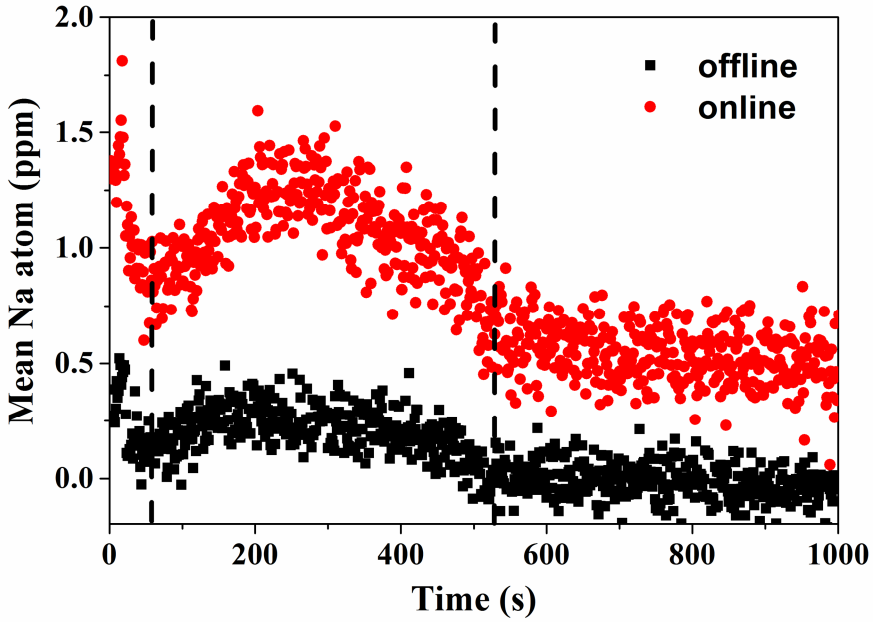

Fig. 3. The average atomic sodium concentration calculated from online and offline measurement results.

530

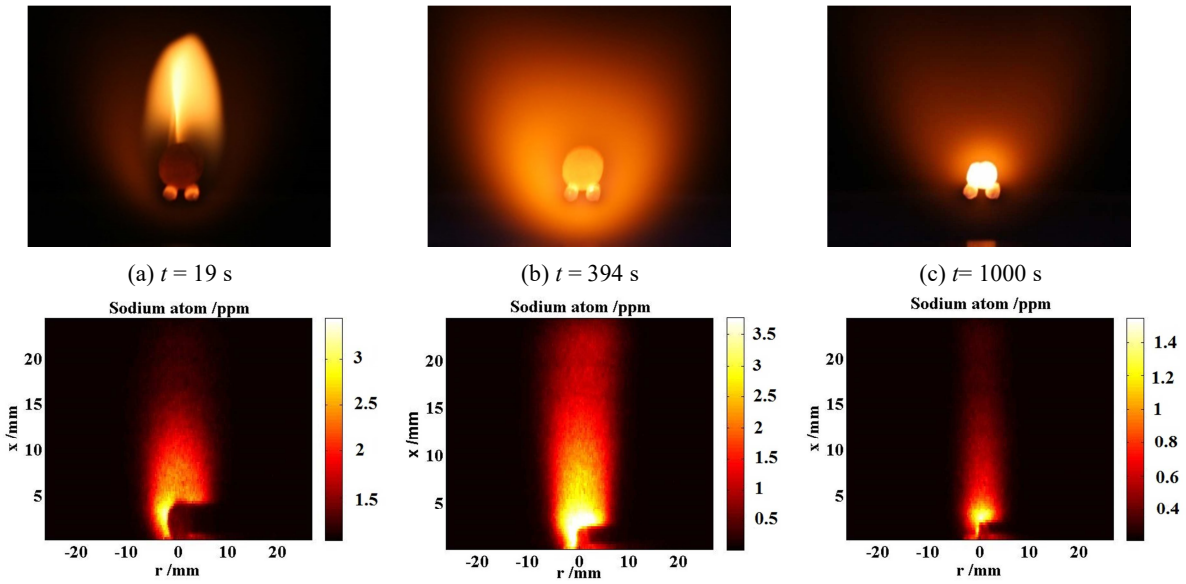

(a) t = 19 s (b) t = 394 s (c) t= 1000 s

(d) t = 19 s (e) t = 394 s (f) t = 1000 s

531 Fig. 4. Imaging of 4-mm coal pellet at various instances in the burning process.(a-c) are the direct imaging of coal
532 combustion at 19, 394 and 1000 seconds respectively while (d-f) are the corresponding sodium atom concentration in
533 ppm.

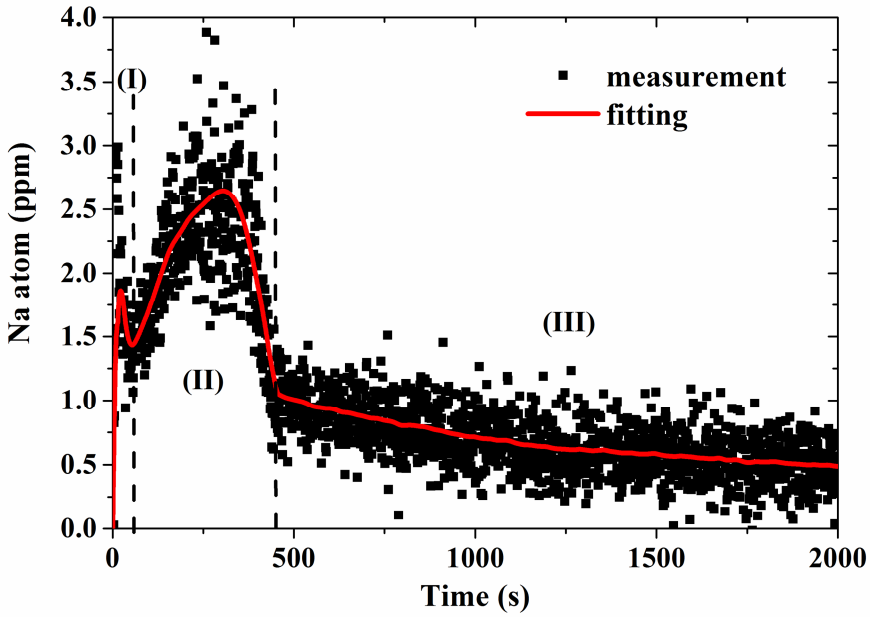

Fig. 5. Temporal concentration profile of Na at a position 14 mm above the 4-mm coal pellet. Vertical dashed lines indicate the separation between the three stages of combustion: devolatilization, char burnout and ash reaction.

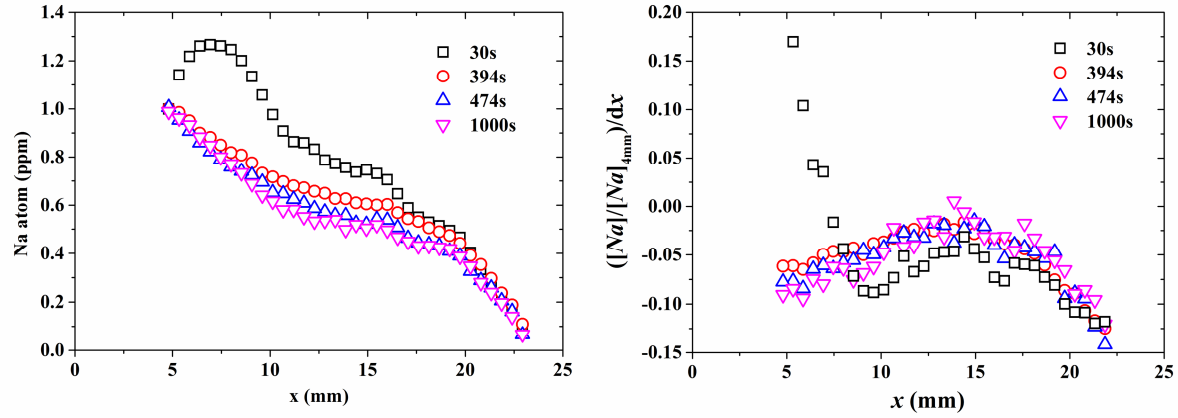

(a) normalized sodium concentrations along the height x (b) x-derivatives of normalized sodium concentrations

Fig. 6. (a) Vertical profile of normalized Na concentration above the 4-mm coal pellet centerline at various times after combustion. (b) first derivative of the vertical profile of normalize Na concentration in (a).

542

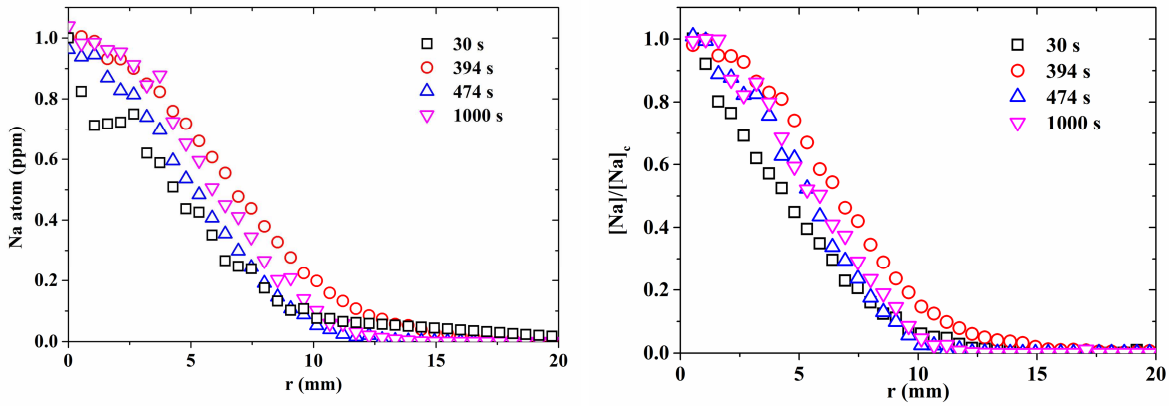

(a) x = 6mm (b) x = 10mm

543 Fig. 7. Single side radial distribution of Na concentration at heights of (a) 6 mm and (b) 10 mm during 4-mm pellet
544 combustion
545

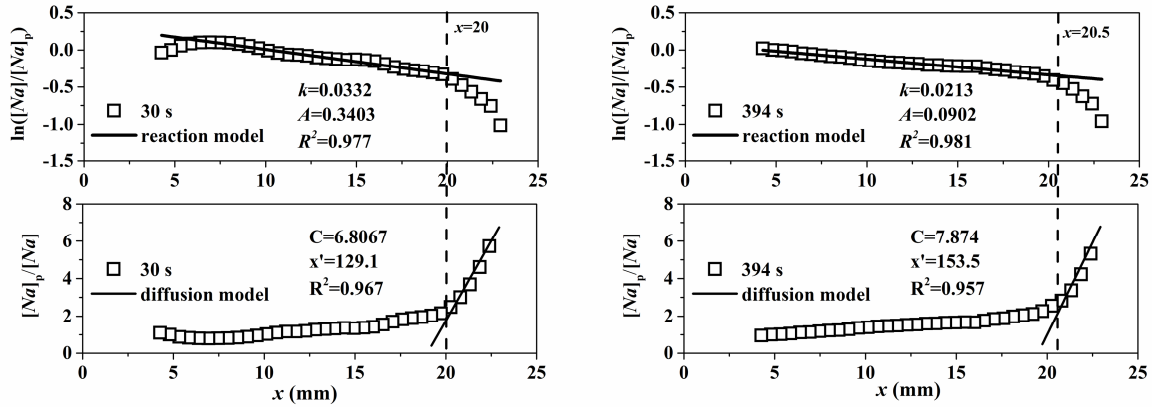

(a) t = 30 s (b) t = 394 s

Fig. 8. Fitting of experimental data to the chemical reaction model and diffusion model from measurements made at (a) t = 30 s and (b) t = 394 s during the combustion of a 4-mm coal pellet.

549

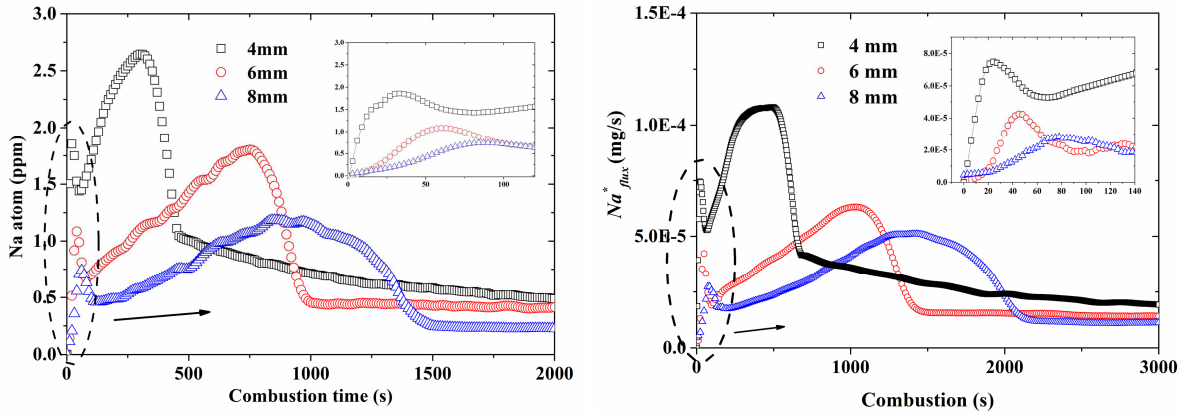

(a) $[Na]$ at x = 14 mm (b) Na^*_{flux} at x = 23 mm

550 Fig. 9. Temporal profile of (a) Na concentration and (b) Na^*_{flux} for coal pellets with the diameter of 4, 6 and 8 mm.

551 Measurement point is located 2 mm above the upper surface of the coal pellet.

552

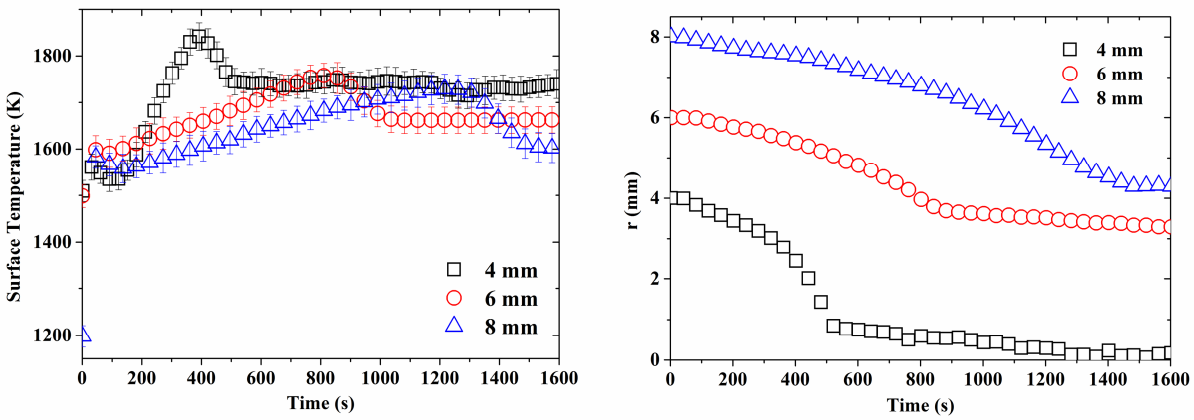

(a) surface temperature (b) diameter

553 Fig. 10. Temporal profile of (a) pellet surface temperature and (b) pellet diameter for coal pellet samples with the
554 diameter of 4, 6, and 8 mm.
555

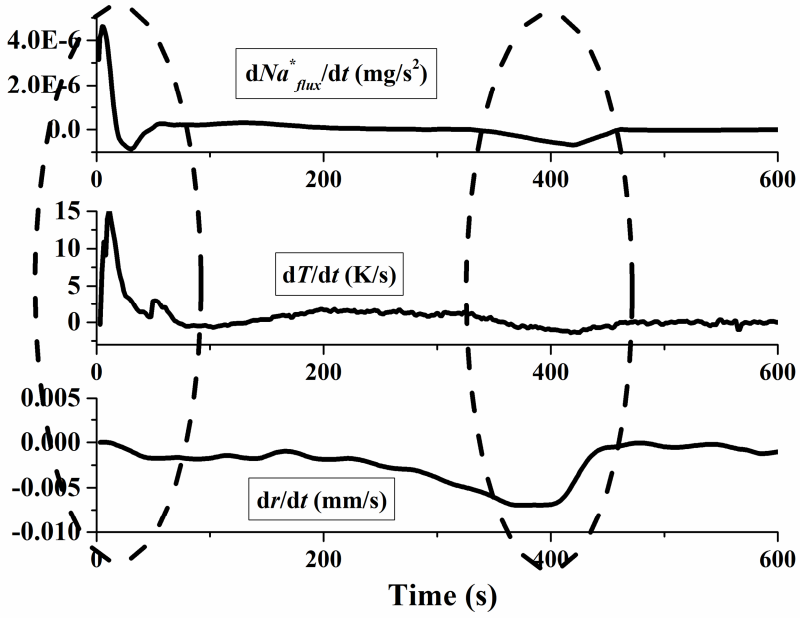

Fig. 11. The derivatives of $Na^*_{flux,t}$, T and d as a function of combustion time.

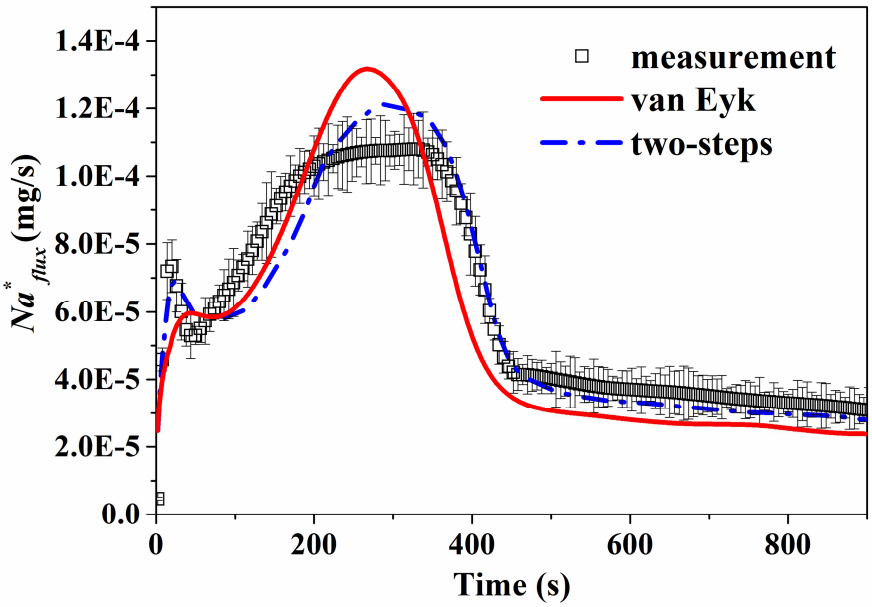

561

562 Fig. 12. Verification of different sodium release kinetics by measurement results.

563